



Combustion Synthesis of Ag Nanoparticles and Their Performance During NaBH₄ Hydrolysis

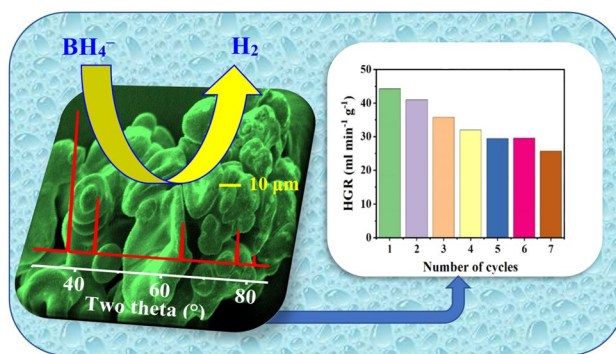
Bahaa M. Abu-Zied¹ · Tarek T. Ali² · Lamia Adly¹

Received: 22 July 2023 / Accepted: 15 January 2024
© The Author(s) 2024

Abstract

Due to their tremendous industrial, environmental, and biological applications, research focusing on the synthesis and applications of silver nanoparticles (Ag NPs) has attracted increased interest from researchers over the past two decades. Their structural as well as textural properties can be easily tuned depending on the synthesis protocol utilized. Combustion synthesis has received increased attention as a one-pot route for the synthesis of a wide spectrum of nanomaterials. In this study, we present the results of synthesizing Ag NPs employing urea as a combustion fuel. The effect of the temperature of calcination on the formation and structural features of Ag NPs has been checked over the 400–700 °C temperature range. The characterization of the synthesized Ag NPs has been performed using XRD, SEM, TEM, and XPS techniques. It was found that Ag NPs, with a crystallite size of 40 nm, start to form at around 400 °C. Conducting the calcination at the 500–700 °C range results in the persistence of the obtained Ag NPs. Moreover, the obtained nanomaterials are characterized by a membrane-like morphology. The activity performance of the synthesized Ag NPs was examined for the hydrolysis of sodium borohydride (NaBH₄) over a temperature range of 35–50 °C. Increasing the calcination temperature has led to a decrease in the activity of the Ag NPs during the NaBH₄ hydrolysis.

Graphical Abstract



Keywords Heterogeneous catalysis · Activation energy · Activity · Calcination · Characterization · Nanotechnology · Preparation and materials

1 Introduction

Metallic nanoparticles (NPs) production is one of the most exciting scientific achievements of the last two decades so far, and it will be of much interest in the future due to their distinctive characteristics, such as small particles' size, their

shapes, and their chemistry, which is reflected in the wide range of their applications [1]. Most of the chemical and physical properties of metallic NPs depend on their size and morphology, which are affected by temperature, period of reaction, concentration, and the ratio of reagents [2]. For these reasons, much attention is currently devoted to the

Extended author information available on the last page of the article

production of the smallest particle size with wonderful morphologies useful in many applications.

Silver NPs have been tremendously investigated due to their superior chemical, physical, and biological characteristics [2–22]; for this reason, they are the focus of our attention in this research. Silver NPs have revolutionized the field of nanotechnology due to their application in several fields that are dependent on unique size-dependent magnetic properties such as physical, chemical, optical, surface Plasmon resonance properties, and electrical resistance. Ag NPs are used in several fields; for instance, Pandey and Ramontja [3] reported antibacterial applications of Ag NPs in biotechnology and biomedical fields. Rajiri et al. [4] demonstrated that Ag NPs have anticancer and therapeutic potential against breast cancer and pancreatic cells. Fayaz et al. [5] addressed the Ag NPs' antimicrobial activity towards gram-positive and gram-negative bacteria. Prasher et al. [6] reported the effectiveness of Ag NPs as drug delivery carriers. Kim et al. [7] synthesized nanosilver and carbon nanocomposite membrane for enhanced water treatment. The various electronic applications of Ag NPs were investigated by Wang et al. [8]. Not only are these mentioned uses for nanosilver, but there are also a lot of uses in our lives, such as bio-sensing [9] and the production of high-performance cotton fabrics [10].

The preparation methods of Ag NPs play a crucial role in their applications because the method of preparation is a key factor in controlling the particles' size and shape, which is reflected in their applications. Numerous routes for Ag NPs synthesis can be found in the open literature. These include chemical etching, sputtering, ball/mechanical milling, thermal/laser ablation, lithography, thermal decomposition, vapor deposition, atomic/molecular condensation, chemical and electrochemical precipitation, the sol–gel process, spray pyrolysis, and biological-based methods [12–17].

The combustion method is one of the most important methods for preparing nanometals because it has quick and easy production, operational simplicity, and the utilization of low environmental impact reagents. In the combustion method, a metallic precursor acts as an oxidizer (normally metal nitrate) that reacts with an organic fuel as a reducing agent (such as sugar, amino acid, urea, ethylene urea, glycine, cetyltrimethylammonium bromide (CTAB), etc.) below a specified degree of combustion temperature to produce metal nanoparticles [23–30]. Several factors impact the properties of nanometals, such as calcination temperature, type of fuel, pH, combustion pressure, the ratio between oxidizer and fuel, and type of solvent. In this way, Sharma et al. [21] showed that, in comparison to glycine, citric acid has the advantage of forming more spherical (diameters of approximately 40 nm) and symmetrical Ag NPs. Spherical Ag NPs parties have also been obtained using gallic acid as a fuel with diameters in the range of 61–400 nm [31].

Employing poly N-vinylpyrrolidone (PVP) and lactic acid as fuels, spherical Ag NPs have been obtained [32]. Moreover, raising the calcination temperature from 350 to 500 °C has led to a particle size increase from 22 to 32 nm of these Ag NPs [32]. A flameless combustion route was used to prepare quasi-spherical Ag NPs with dimensions in the 20–30 nm range, starting with cellulose nitrate and silver carbonate at 350 °C [33].

Reviewing the available literature resources revealed a growing interest in the Ag NPs synthesis in general and utilizing the combustion route in particular. In the open literature, there is a lack of knowledge regarding the usage of urea as a combustion fuel during Ag NPs synthesis. Therefore, the present research involves a systematic investigation that addresses the role of the combustion fuel (urea) as well as the calcination temperature (400–700 °C) on the formation of Ag NPs. Various characterization tools will be devoted to the precise elucidation of the crystal structure, the morphologies, and the surface properties of the as-prepared Ag NPs. Finally, the activity of the formed nanomaterials will be evaluated for NaBH₄ decomposition.

2 Experimental

2.1 Combustion Procedure

Analytical-grade precursors of the oxidized (silver nitrate, AgNO₃) and the organic fuel (urea, CH₄N₂O₂) were used as received. One materials series has been prepared that focuses on the effect of the temperature of calcination on the phase formed, crystallite size, and morphology of Ag NPs. In this series, the fuel/oxidizer ratio was adjusted to 0.50, and the calcination temperature was selected at 400, 500, 600, and 700 °C. The precursors have been dissolved in the least amount of distilled water, mixed, and dried gently over a hotplate. The furnace was adjusted to the desired temperature (500–700 °C). Then, the dried materials were, finally, subjected to calcination at that temperature in static air for 1 h. The produced solids have been referred to by the abbreviation Ag-x, where the x-value denotes the temperature of calcination.

2.2 Characterization Tools

Powder X-ray diffraction patterns have been performed on monochromatized Cu-K α radiation ($\lambda = 0.154060$ nm). The operation condition used was 30 kV and 30 mA with a scanning rate of 0.02136° s⁻¹. Morphology identification of some selected Ag NPs was performed using scanning and transmission electron microscopies. The models used were JEOL (JSM-5400 LV) and (JEMTH-100 II), respectively. In the scanning mode, the samples have been measured

after performing gold sputtering. Before the transmission inspection, the samples have been sonicated (for 30 min), loaded on Cu-grid, and left to dry. Surface inspection using the XPS technique has been examined on the K-ALPHA (Thermo Fisher Scientific) instrument. The conditions utilized were monochromatic X-ray Al K-alpha radiation, spot size 400 μm , binding energy (BE) range (10 to 1350 eV), and pressure of 1×10^{-9} m bar. The C 1 s peak (at 284.8 eV) was used for calibrating the binding energies in the XPS spectra.

2.3 Activity Assessment

The hydrolysis of NaBH₄ experiments over the various Ag NPs was conducted in a 100 ml flask reactor made of Pyrex glass, whereas the volume of the produced hydrogen was measured using the water displacement method [34]. The reactor was immersed in a 1 L Pyrex glass beaker. The temperature of the reactor was controlled and monitored using an IKA-RCT hotplate connected to a contact thermometer. 0.1 g Ag catalyst was introduced to the reactor, which contains a thermostated 20 ml NaBH₄ solution (1.5 wt%). The reaction started, and the generated hydrogen volume was followed up by the water displacement method over a reaction temperature range of 35–50 °C.

3 Results and Discussion

3.1 Phase Formation

The recorded X-ray powder diffraction patterns over the 2θ range of 20–90° are presented in Fig. 1. The obtained pattern for the 400 °C calcined samples reveal the crystalline nature of this sample, together with the presence of a large number of peaks. Analyzing these peaks revealed the presence of major peaks at $2\theta = 21.74^\circ, 24.34^\circ, 29.70^\circ, 31.93^\circ, 32.82^\circ, 39.12^\circ, 40.13^\circ, 43.52^\circ, 46.25^\circ, 49.77^\circ,$ and 53.87° . These peaks match those of orthorhombic AgNO₃ as a major phase (JCPDS file No. 00-006-0363). However, these peaks showed a slight 2θ shift of 0.05–0.12° towards higher values. In this context, it is to be mentioned that the various reported JCPDS peaks of AgNO₃ vary in the range of 0.70° from each other. The detection of such a phase agrees well with the reported data for the complete decomposition of silver nitrate at approximately 500 °C [35]. An additional factor can be raised by analyzing the rest of the peaks in this sample. Another peak can be observed at $2\theta = 38.18^\circ, 44.35^\circ, 64.51^\circ, 77.45^\circ,$ and 81.61° , which could be anticipated to be the presence of a minor amount of Ag (JCPDS file No. 01-089-3722). A trace amount of carbon can also be determined by the presence of the reflections at $2\theta = 44.35^\circ$ and 75.22° (JCPDS file No. 00-001-1249).

Therefore, it is reasonable to relate the observed slight shift in the 2θ values of AgNO₃ to the presence of these phases. In other words, the co-existence of the Ag and C phases in the constituents of the Ag-400 sample could be responsible for a slight d-spacing shift. In this context, Wu et al. [36] reported a shift in the peak positions of their Ag NPs prepared by the hydrothermal route. Singh and Khanna [37] reported a little change in the Ag NPs lattice spacing from 2.365 to 2.382 Å because of increasing the Ag loading from 2 to 10% in their Ag/polymethylmethacrylate (PMMA) composite. Considering the thermal decomposition of urea, it proceeds with the formation of a wide spectrum of products, including biuret, cyanuric acid, cyanic acid, ammonia, ammonium cyanate, cyanamide, ammelide, ammeline, and melamine [23, 38–41]. The reaction covers a wide range of temperatures (from > 130 °C to approximately 400 °C) with complex reaction pathways [23, 38–41]. Krum et al. [40] demonstrated that bare urea undergoes full decomposition after isothermal heating at 380 °C for 55 h. This agrees well with our XRD data for the Ag-400 sample, where only a trace amount of carbon was found in that sample.

Raising the temperature of calcination from 400 to 500 °C is associated with the disappearance of all the previously mentioned peaks due to AgNO₃ and C phases and the development of the five peaks located at $2\theta = 38.03^\circ, 44.19^\circ, 64.31^\circ, 77.29^\circ,$ and 81.40° . These peaks could be allocated to the (111), (200), (220), (311), and (222) planes of the cubic Ag (space group Fm-3m, JCPDS file No. 01-089-3722), respectively. Increasing the temperature of calcination to 700 °C resulted in the persistence of these five peaks, indicating the detection of only one phase, viz., Ag NPs. It can be stated that within the examined temperature range, Ag NPs represent the only phase detected during the 500–700 °C range. The crystallite size of the formed Ag NPs, within the calcination temperature range of 500–700 °C, has been calculated using the Scherrer equation employing the (111) reflection, which is usually used for estimating the silver crystallite size [14, 36, 37]. The obtained values were 40, 37, and 36 nm for the Ag-500, Ag-600, and Ag-700 samples, respectively. Two points could be raised here: (i) these values show only a very slight decrease with increasing the calcination temperature, and (ii) the estimated values were higher than those resulting from silver acetate thermal degradation (13–22 nm) [14] and silver in Ag/PMMA composite (23–25 nm) [37] and lower than those reported for Ag NPs prepared using PVP (78–113) [36]. Using in situ X-ray diffraction, Yanase et al. [42] reported that on heating metallic silver in an oxygen atmosphere, the silver lattice becomes more stressed, which eventually leads to failure and a decrease in crystallite size. Nagy and Mestl [43] reported a striking reduction in the silver crystallite size during the time on stream experiments on treating silver catalyst in 10

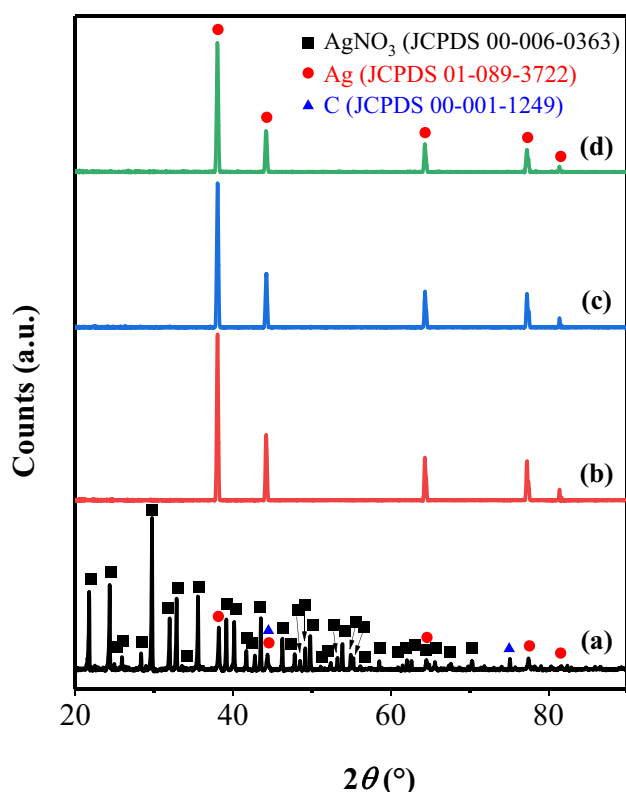


Fig. 1 The recorded X-ray patterns for the silver-urea precursor calcined at 400 (a), 500 (b), 600 (c), and 700 °C

Vol.% oxygen at 750 °C. They suggested that this decrease is due to the formation of interstitially located bulk-dissolved oxygen species. TPO experiments suggested the presence of the $\text{Ag} \rightarrow \text{Ag}_2\text{O} \rightarrow \text{Ag}$ redox cycle on heating Ag-based catalysts over the temperature range of 375–625 °C [44]. Based on nonisothermal TGA-DTA measurements, chemisorbed oxygen on Ag was released via an exothermic peak at 700–780 °C [45]. Hong et al. [46] reported an Ag structure deterioration for the CrN_x/Ag nanocomposite (20.2 at.% Ag) calcined at 800 °C. Based on these literature data, it is plausible to attribute the observed slight crystallite size decrease of Ag NPs decrease with increasing calcination temperature (Fig. 1) to the formation of bulk-dissolved oxygen species, formed during calcination in air, which results in the deterioration of metallic silver structure with temperature.

3.2 Characterization of Ag NPs

In the preceding section, it was found that the reaction between the mixture constituents (AgNO_3 and $\text{CH}_4\text{N}_2\text{O}_2$) takes place at 500 °C. Therefore, and in combination with the activity data (vide infra), Ag-500 and Ag-700 catalysts

have been subjected to characterization using SEM, TEM, and XPS techniques. The obtained micrograph for the Ag-500 catalyst (Fig. 2a) shows a compact arrangement of particles with sphere-like morphology and sizes ranging from 5 to 20 μm . Various pores can be observed, ascribable to the various gases released accompanying the precursor's combustion. It is evident that increasing the calcination temperature to 700 °C is associated with particle welding (Fig. 2b), which leads to the loss of the sphere-like particles of the Ag-500 catalyst. The Ag-700 catalyst shows clear evidence of particle welding, as indicated by the arrows, where the various particles are linked to each other, forming bigger ones. The morphology of the Ag-700 catalyst is similar to that observed for other Ag NPs prepared via hydrogen reduction of Ag_2O [47], the solvothermal method [48], and thermal decomposition of silver acetate [14].

TEM images of Ag-500 and Ag-700 catalysts are shown in Fig. 3, which are magnified by a factor of 19 kx. For both catalysts, abundant pores are distributed among the Ag NPs, giving a membrane-like network. The image of Ag-500 catalysts (Fig. 3a) shows a set of two-layered membranes with elongated pores. In this context, silver-based membranes have been previously reported in the literature and have important energy applications [49, 50]. With the aid of the XRD findings and TEM inspection, we may suggest the following reasons for Ag NPs formation. First, Wu et al. [36] reported that the viscosity increase of the water–ethanol solution retards the Ag^+ ion diffusion, which is associated with an anisotropic growth of Ag nanocrystals. Knowing that the viscosity of the urea–water solutions is higher than that of pure water [51]. Thus, we may suggest that one role of urea is to reduce silver ions diffusion, which favors the anisotropic growth of Ag NPs with membrane-like morphology up on the precursor decomposition. Second, it is generally agreed that, among the Ag nanocrystal planes, the (1 1 1) plane processes the lowest surface energy [36, 52, 53]. This plane tends to adsorb molecules such as polymers and ammonia, which results in additional surface energy lowering on this plane [36, 52]. Therefore, it is reasonable to propose that during the precursor preparation, the urea molecules are adsorbed on the (1 1 1) plane, leading to a decrease in both its surface energy and its growth rate. This, in turn, would lead to lower adsorption of urea on other faces, leading to a higher growth rate, which favors the formation of the 2D morphology upon precursor decomposition. A similar argument was used to interpret the formation of Ag NPs with plate-like morphology [36, 52]. Increasing the calcination temperature results in noticeable morphological modifications. The photograph of the Ag-700 catalyst (Fig. 3b) indicates the

presence of a porous membrane of Ag NPs with smaller diameters and wider distribution. Moreover, the pores show a decrease in size either by splitting into smaller pores (as shown by the α -arrows) or via pore narrowing (as shown by the β -arrows), which eventually leads to pore blocking as shown by the γ -arrows. From the electron microscopy examinations, it is obvious that, in addition to the role of the precursors (type of fuel and fuel/oxidizer ratio [21]), the calcination temperature plays a crucial role in adjusting the morphology and texture of the prepared Ag NPs.

Based on the activity assessment, the Ag-500 and Ag-700 samples were further investigated using XPS analysis. In the survey spectra of both catalysts (not shown), only silver, oxygen, and carbon elements have been detected; no other element, such as nitrogen, was detected on the surface of both catalysts. The detection of carbon at the surface of both silver samples is not surprising, which probably originated from the urea decomposition. In this context, the detection of both O and C has been reported for the Ag NPs obtained from the degradation of silver acetate [14]. The fitted Ag 3d XPS spectrum of the Ag-500 catalyst is shown in Fig. 4a. Two peaks located at 368.15 and 374.10 eV with a splitting BE of approximately 6 eV can be seen in the original spectrum. From the literature database, these peaks could be indexed to Ag 3d_{5/2} and Ag 3d_{3/2} electronic levels, respectively [14, 20, 22, 54–56]. Peak deconvolution of the

Ag 3d_{5/2} level yields three features at 367.61, 368.11, and 369.29 eV. Similar features can be obtained by the peak fitting of the Ag 3d_{3/2} level, which appear at 373.13, 374.12, and 375.32 eV. For Ag 3d_{5/2} and Ag 3d_{3/2} electronic levels, the sharp peaks at 368.11 and 374.12 eV and the weak ones at 369.29 and 375.32 eV could be assigned to the metallic silver [14, 20, 54–56]. It was reported that oxidizing metallic silver is associated with a binding energy lowering of both levels [14, 54]. Therefore, the small-intensity features at 367.61 and 373.13 eV, respectively, could be related to the presence of Ag⁺ species, in the form of Ag₂O, at the surface of the prepared nanomaterial [14, 20, 54]. The detection of Ag⁺ species agrees with the work of Sun et al. [55], who observed the development of a minor amount of oxidic silver in their Ag/graphene composites. Their formation was attributed to the possible partial Ag NPs oxidation upon exposure of the prepared composites to atmospheric air [55]. Consistent data were reported by Albiter et al. [56], who detected Ag₂O on the surface of the Ag/TiO₂ photocatalyst via Ag⁰ oxidation upon exposure to the air environment.

Peak-deconvolution of the O 1s core level of the Ag-500 catalyst (Fig. 4b) gives two peaks at BEs of 530.85 and 531.78 eV. The first peak could be indexed to the lattice oxygen of Ag₂O, whereas the second peak could be indexed to the surface hydroxyl oxygen and/or C=O groups [14, 20, 54, 57]. Three features can be seen in the deconvoluted

Fig. 2 SEM micrographs obtained for Ag-500 (a) and Ag-700 (b) catalysts

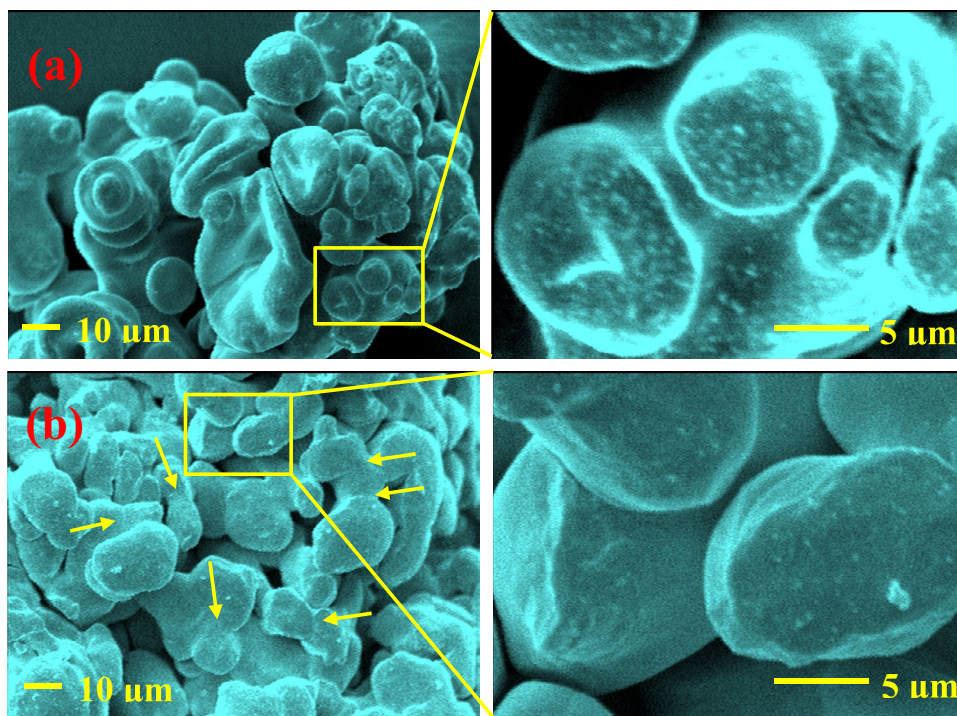
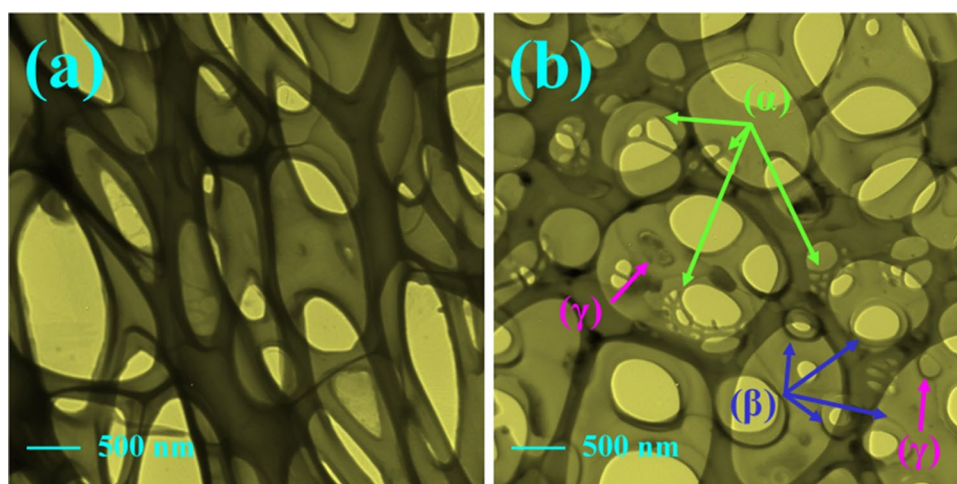


Fig. 3 TEM micrographs obtained for Ag-500 (a) and Ag-700 (b) catalysts



asymmetric C 1s core level of the Ag-500 catalyst (Fig. 4(c)), which suggests the existence of various carbon-containing function groups at the prepared Ag NPs. The first one, which is located at 284.68 eV, may be due to C–H and/or C=C bonding [14, 57]. The second feature appearing at BE of 285.22 eV could be indexed to C–O and/or C–C bonding [14, 57]. The lowest intensity peak observed at BE 287.79 eV could be assigned to C=O bonding [14, 57].

The deconvoluted Ag 3d, O 1s, and C 1s core levels of the Ag-700 catalyst are presented in Fig. 5. The same species identified in the case of the Ag-500 catalyst can be identified here. However, some modifications can be identified. The intensity of the Ag 3d spectrum of the Ag-700 catalyst (Fig. 5a) shows a noticeable decrease. Meanwhile, the relevant XPS spectra of O 1s (Fig. 5b) and C 1s (Fig. 5c) reveal a noticeable intensity decrease. A quantitative analysis of the three elements at the surface of both catalysts can be seen in Table 1. It is reasonable to correlate the obtained decrease in the C and O concentrations of Ag-700 catalyst with the expected increased burning rate of the carbonaceous species located at its surface upon increasing the calcination temperature. It is to be mentioned that the first peak intensity in the fitted spectrum of C 1s of the Ag-700 catalyst is higher than those of the other two peaks (Fig. 5c). This indicates that the surface of this sample has a higher content of C–H and/or C=C species.

It is obvious from Figs. 4 and 5 that the intensity of the main peak assignable for metallic silver is higher than that of Ag⁺ for both Ag-500 and Ag-700 catalysts. It is plausible to suggest that, however, no diffraction peaks were observed for silver oxide phases in the XRD patterns of both catalysts. The XPS detected Ag⁺ species suggests that a portion of the formed metallic silver is oxidized by the atmospheric oxygen, yielding surface Ag₂O at the surface of the prepared Ag NPs.

3.3 NaBH₄ Hydrolysis Activity

Figure 6 shows the results of NaBH₄ hydrolysis experiments (V_{H_2} vs. time) for the Ag NPs calcined at 500, 600, and 700 °C. It can be seen that, all over the tested reaction temperatures (35–50 °C), there is no induction (or activation) period. In other words, there was no considerable hydrogen generation at the beginning of the reaction. Moreover, a linear dependence of the produced hydrogen volume with time can be observed. Furthermore, a continuous activity increase is associated with an increase in the reaction temperature. The obtained activity order is Ag-500 > Ag-600 > Ag-700. For instance, 35.2, 38.5, and 44.5 min are required for producing 75 ml of hydrogen at 35 °C over Ag-500, Ag-600, and Ag-700 catalysts, respectively. This indicates that the HGR significantly depends on the catalyst calcination temperature. All over the tested reaction temperatures, a continuous HGR decrease with the calcination temperature can be seen.

The rate constants and the activation energies of the NaBH₄ hydrolysis over the three Ag catalysts can be computed from the obtained data. The hydrogen generation rate (HGR) has been computed from the slopes of the V_{H_2} vs. time curves, and the obtained values are shown in Fig. 7a. It is obvious that the HGR responds positively to the reaction temperature and negatively to the calcination temperature. The highest values (21.5, 32.2, 57.6, and 70.7 ml min⁻¹ g⁻¹ at 35, 40, 45, and 50 °C, respectively) are obtained over Ag-500 at 50 °C. These HGRs are much lower compared to those of Co₃O₄/C (1821 ml min⁻¹ g⁻¹ at 35 °C) [34], Co/CNTs (410 ml min⁻¹ g⁻¹ at 35 °C) [57], CoB (1735 ml min⁻¹ g⁻¹ at 20 °C) [58], Co thin films (7900 ml min⁻¹ g⁻¹ at 25 °C) [59], and Co₃O₄ NPs (1776 ml min⁻¹ g⁻¹ at 25 °C) [60]. These catalysts are known to show excellent activity for this reaction. On the other hand, they lie approximately

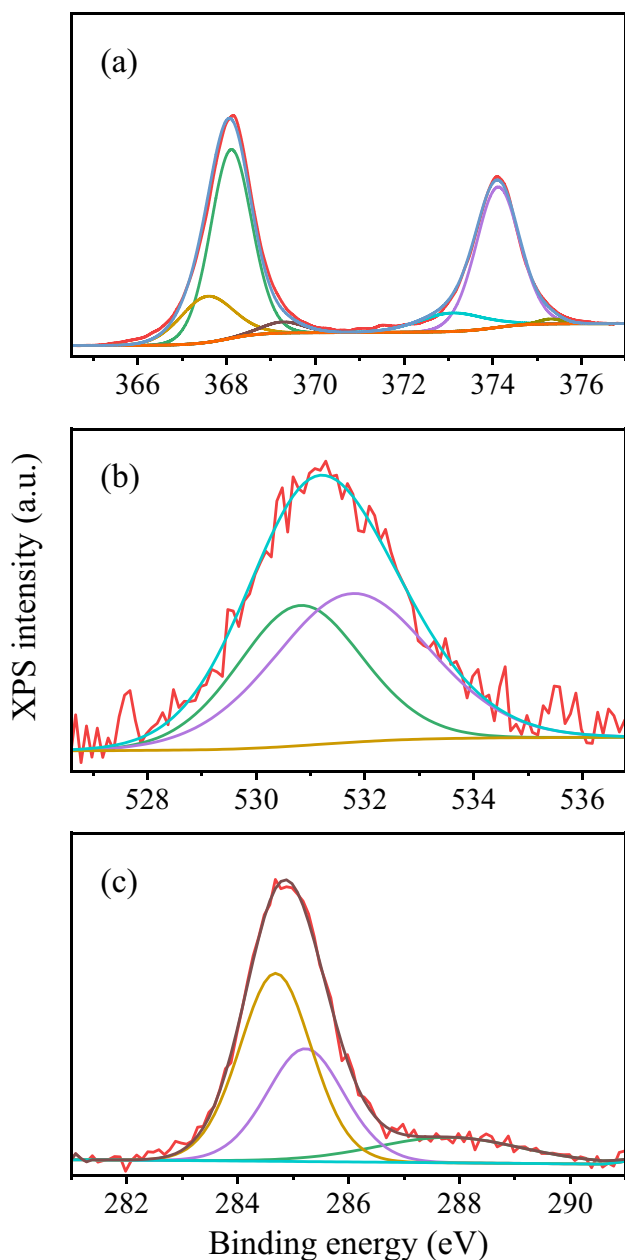


Fig. 4 Fitted Ag 3d (a), O 1 s (b), and C 1 s (c) XPS spectra of Ag-500 catalyst

within the same activity range for the reaction performed over Pd/MWCNs ($20.7 \text{ ml min}^{-1} \text{ g}^{-1}$ at $30 \text{ }^\circ\text{C}$) [61], Ag/MWCNs ($17.4 \text{ ml min}^{-1} \text{ g}^{-1}$ at $30 \text{ }^\circ\text{C}$) [62], Ru/Al₂O₃ ($34.9 \text{ ml min}^{-1} \text{ g}^{-1}$ at $25 \text{ }^\circ\text{C}$) [63], and chitin/Cu hydrogel nanocomposite (23.8 and $46.2 \text{ ml min}^{-1} \text{ g}^{-1}$ at 35 and $55 \text{ }^\circ\text{C}$, respectively) [64]. Regarding the effect of the calcination temperature on the activity performance, Durano et al. [60], working on Co₃O₄ NPs calcined at 600 – $800 \text{ }^\circ\text{C}$, reported the highest activity for the $700 \text{ }^\circ\text{C}$ calcined Co₃O₄ NPs. They ascribed the poor activity of the $800 \text{ }^\circ\text{C}$ calcined catalyst to the active sites' destruction at such a high temperature.

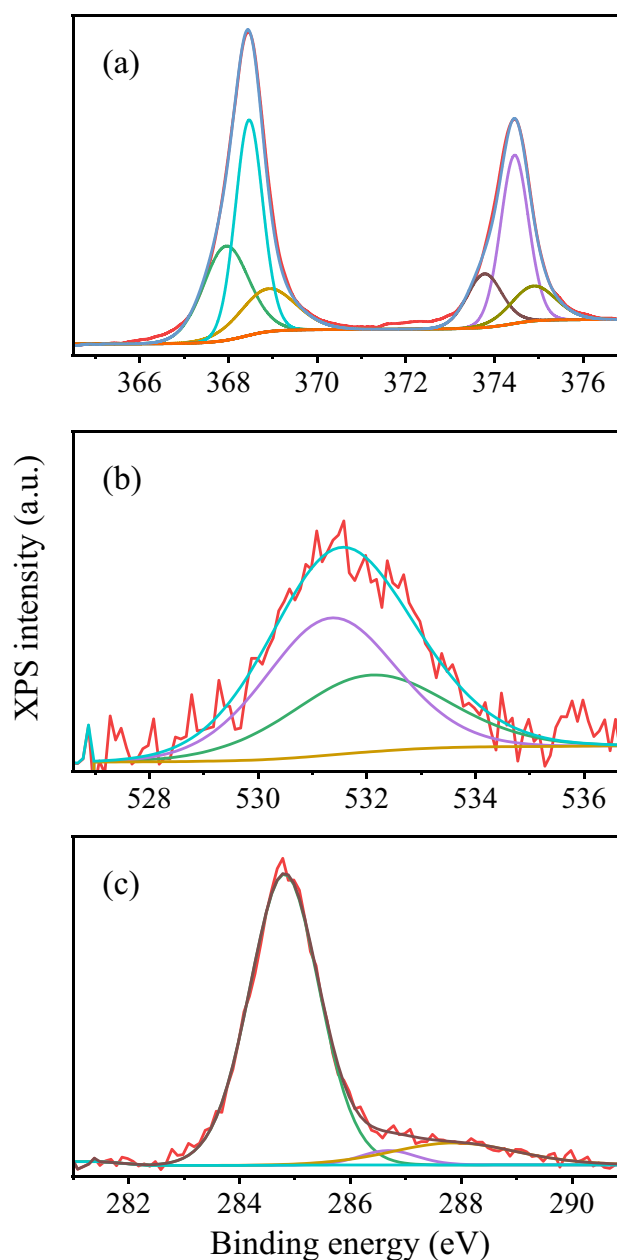


Fig. 5 Fitted Ag 3d (a), O 1 s (b), and C 1 s (c) XPS spectra of Ag-700 catalyst

Table 1 XPS surface binding energies and atomic percentages of silver, oxygen, and carbon of Ag-500 and Ag-700 catalysts

Element	Ag-500		Ag-700	
	BE (eV)	Atomic %	BE (eV)	Atomic %
Ag	368.15	28.86	368.44	37.21
O	531.30	16.87	531.58	14.34
C	284.88	54.27	284.78	48.45

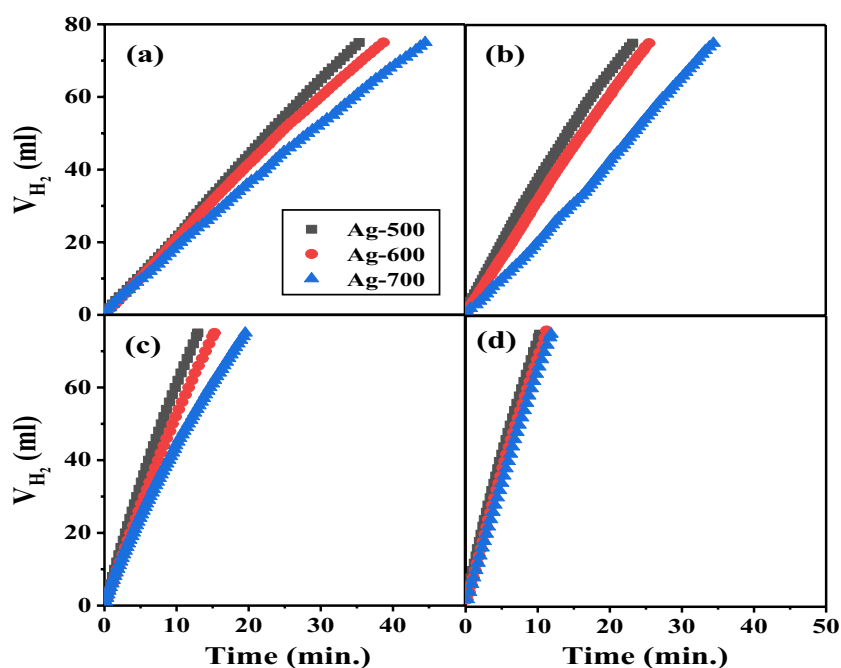
For $\text{Co}_3\text{O}_4/\text{C}$ hierarchical nanocomposites, the highest HGR was obtained over the 500 °C calcined catalyst [34]. Higher calcination temperatures are associated with a decrease in the textural parameters and the active centers. In the present work, it seems that 500 °C is the optimal temperature for the formation of Ag NPs and their highest performance for NaBH_4 hydrolysis.

Applying the Arrhenius equation, $\ln k = \ln(A) - (E_a/RT)$, to the data presented in Fig. 7a, enables the calculation of the activation energies for the hydrolysis reaction for the three catalysts. Figure 7b depicts the dependence of \ln HGR vs. the reciprocal absolute temperatures. Good linearity can be seen for all catalysts. By the compensation in the Arrhenius equation, the computed activation energies were 68.8, 69.9, and 74.8 $\text{kJ mol}^{-1} \text{K}^{-1}$ for Ag-500, Ag-600, and Ag-700 catalysts, respectively. By plotting $\ln A$ vs. E_a , for the three Ag catalysts, the Constable plot can be obtained as indicated in Fig. 7c. Good linearity can be seen with a positive slope, which belongs to case “A” of Bond’s et al. classification [65]. This, in turn, highlights the presence of a compensation effect among these catalysts. In other words, hydrogen is generated over these Ag NPs catalysts from the same active sites and via the same mechanism.

Four kinetic steps have been reported for the catalyzed hydrolysis of NaBH_4 , which implies the adsorption of

both NaBH_4 and H_2O on active metal sites [34, 57, 61, 62, 66–68]. In the first step, BH_4^- ion is chemisorbed on the active site, which is followed by the H^- ion transfer to another active site. In the third step, hydrogen is evolved via the reaction between the adsorbed H^- and H_2O , leaving behind OH^- ion. The final step involves the reaction of OH^- with the adsorbed BH_3 , forming the $\text{BH}_3(\text{OH})^-$ ion. The formed $\text{BH}_3(\text{OH})^-$ undergoes successive cycles of reactions, eventually leading to the formation of $\text{B}(\text{OH})_4^-$. The desorption of such a product leads to the regeneration of the active center. Huff et al. [62] reported the mechanism for the NaBH_4 hydrolysis over AgMWCNs, indicating the role of silver in the interaction with the BH_4^- ion. However, they did not indicate the role of silver species or the type of active centers in the BH_4^- and H_2O adsorption and reaction. Based on XPS investigations for the NaBH_4 hydrolysis over Co-B [66] catalysts, it was concluded that the electron-enriched metal is crucial, which is responsible for facilitating the reaction by providing the required electrons. In the proposed mechanism by Andrieux et al. [67], BH_4^- and H_2O are adsorbed on atoms “A” and “B”, respectively. Atom “A” is an electron-rich center that can donate its electron density to the boron atom. On the other hand, atom “B” is an electron-deficient center that attracts the electron density of the oxygen atom in the water molecule. Over the Co

Fig. 6 Activity measurements in terms of V - t plots obtained for the Ag-500, Ag-600, and Ag-700 catalysts at 35 °C (a), 40 °C (b), 45 °C (c), and 50 °C (d)



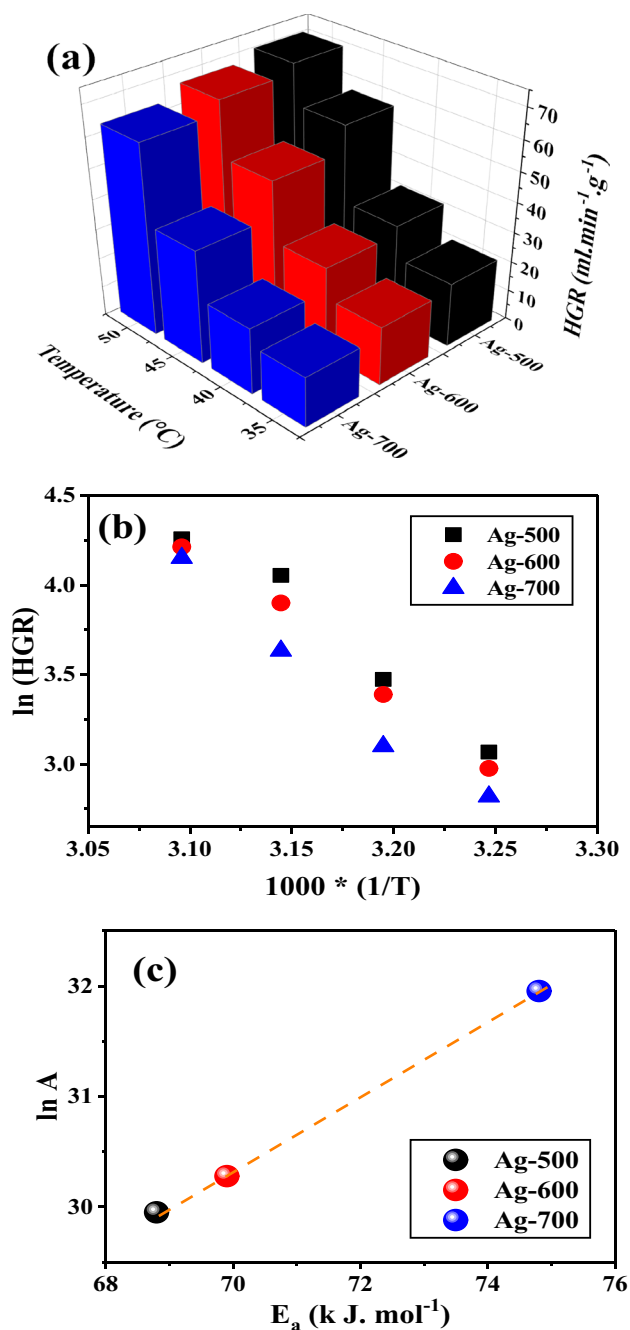


Fig. 7 **a** Dependence of the hydrogen generation rate (HGR) on the reaction temperature, **b** Arrhenius plots, and **c** Constable-plot obtained for Ag-500, Ag-600, and Ag-700 catalysts

NPs catalyst, atoms “A” and “B” have been proposed to be Co⁰ and Co^{δ+}, respectively [67]. Over Co/MWCNTs and hierarchical Co₃O₄/C NPs, these atoms were suggested to be the Co²⁺ and Co³⁺ species, respectively [34, 57]. Over Ru-RuO₂/C catalyst, Ru⁰ and RuO₂ have been suggested as adsorption sites for BH₄⁻ and H₂O, respectively [68]. Our XPS analysis revealed the presence of Ag⁰ and Ag⁺, as indicated by the peak deconvolution of the 3d electronic

level (Figs. 4a and 5a), on the surface of Ag-500 and Ag-700 catalysts. Accordingly, it is plausible to assign these species as electron-rich and electron-deficient adsorption sites, respectively. Moreover, it was found that increasing the temperature of calcination from 500 to 700 °C is associated with an increase in the BE of Ag metal (Table 1). In other words, the lower binding energy of Ag metal in the Ag-500 catalyst indicates a higher electron density on Ag NPs, which could be the reason for the higher activity of the Ag-500 catalyst compared to the Ag-700 catalyst.

The reusability tests have been performed for seven cycles. The obtained *V-t* plots vs. time and the HGR vs. the number of cycles for the NaBH₄ hydrolysis over the optimal catalyst, i.e., Ag-500, are shown in Fig. 8 (conditions: 1.5 wt% NaBH₄, 0.2 g catalyst, 40 °C reaction temperature).

It can be seen that the activity decreases gradually with cycles. However, the magnitude of this decrease is less after

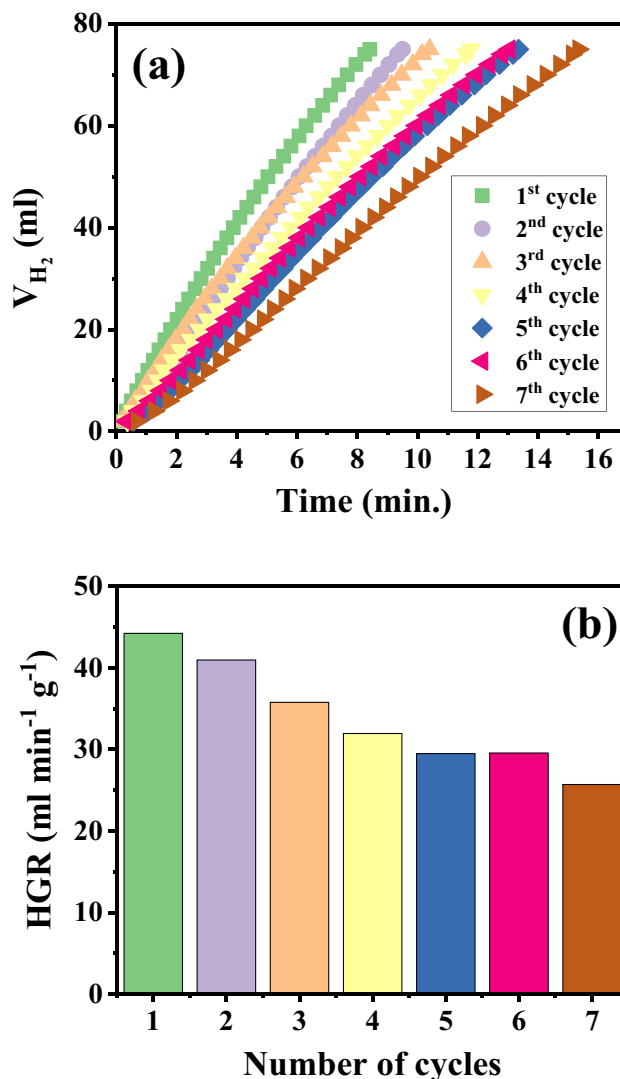


Fig. 8 Recycling tests: **a** *V-t* plots versus time and **b** HGR versus number of cycles performed using Ag-500 catalyst

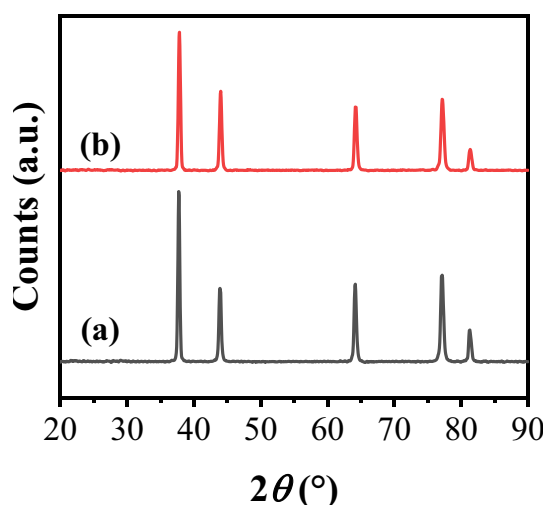


Fig. 9 XRD patterns of the spent Ag-500 and Ag-700 catalysts after seven cycles of the catalytic activity tests

the 4th cycle. The catalyst is still showing 67 and 58% of its initial activity after the 4th and 7th cycles, respectively. This activity decrease agrees with that reported for other catalysts. For instance, around 70% retaining of the initial activity was reported for the NaBH_4 hydrolysis after five cycles over hierarchical Co_3O_4 /carbon NPs [34], $2.8\text{CoB}/\text{Ag-TiO}_2$ [58], and cobalt-based thin films (14%) [59]. Lower activities have been reported over other catalysts such as Co/MWCNTs (34%) [57] and intrazeolite Co^0 nanoclusters (59%) [69]. This activity decrease could be ascribed to: (i) the development of strongly adsorbed borate complex; (ii) the induced structural and/or morphological modifications in the catalysts [57]; and (iii) the possible loss of the catalyst during recycling.

Figure 9 shows the XRD patterns for the Ag-500 and Ag-700 spent catalysts after seven catalytic cycles. In comparison with the fresh catalysts, it is evident that the spent ones still possess reflections due to the cubic Ag (space group $\text{Fm-}3\text{m}$, JCPDS file No. 01-089-3722) indicating that the structure remained intact after contact with NaBH_4 for several runs.

4 Conclusions

Based on the previous findings, we may suggest the following points: The combustion route, using urea as a fuel, is a novel one-pot technique for preparing Ag NPs, which adopt the cubic structure and have a crystallite size in the range of 36–40 nm. The role of the used combustion fuel is not only to minimize the temperature required for phase formation but also to favor the reduction of silver ions and act as a structure-directing agent for morphology control. The prepared Ag NPs are characterized by a porous structure with

a membrane-like morphology. No diffraction peaks were observed for silver oxide phases in the XRD patterns. However, Ag^+ species were detected at the surface of the prepared Ag NPs using XPS investigation. The activity of the prepared nanomaterials was evaluated for NaBH_4 hydrolysis. The 500 °C calcination temperature represents the balance temperature for the formation of Ag NPs and their highest activity performance. Finally, in addition to its catalytic application for the NaBH_4 hydrolysis, the porous morphology nominates the prepared Ag NPs for the application(s) as a membrane.

Funding Open access funding provided by The Science, Technology & Innovation Funding Authority (STDF) in cooperation with The Egyptian Knowledge Bank (EKB).

Data Availability Raw data files of the present article are available from the corresponding author upon reasonable request.

Declarations

Conflict of interest The authors have no relevant financial or non-financial interests to disclose.

Open Access This article is licensed under a Creative Commons Attribution 4.0 International License, which permits use, sharing, adaptation, distribution and reproduction in any medium or format, as long as you give appropriate credit to the original author(s) and the source, provide a link to the Creative Commons licence, and indicate if changes were made. The images or other third party material in this article are included in the article's Creative Commons licence, unless indicated otherwise in a credit line to the material. If material is not included in the article's Creative Commons licence and your intended use is not permitted by statutory regulation or exceeds the permitted use, you will need to obtain permission directly from the copyright holder. To view a copy of this licence, visit <http://creativecommons.org/licenses/by/4.0/>.

References

- Khan I, Saeed K, Khan D (2019) Nanoparticles: properties, applications and toxicities. *Arab J Chem* 12(7):908–931
- Xu R, Wang D, Zhang J, Li Y (2006) Shape-dependent catalytic activity of silver nanoparticles for the oxidation of styrene. *Chem Asian J* 1:888–893
- Pandey S, Ramontja J (2016) Sodium alginate stabilized silver nanoparticles–silica nanohybrid and their antibacterial characteristics. *Int J Biol Macromol* 93(Pt A):712–723
- Rajiri MS, Aminsalehi M, Shahbandeh M, Maleki A, Jonoubi P, Rad AC (2021) Anticancer and therapeutic potential of *Delonix regia* extract and silver nanoparticles (AgNPs) against pancreatic (Panc-1) and breast (MCF-7) cancer cell. *Toxicol Environ Health Sci* 13:45–56
- Fayaz AM, Balaji K, Girilal M, Yadav R, Kalaichelvan PT, Venketesan R (2010) Biogenic synthesis of silver nanoparticles and their synergistic effect with antibiotics: a study against gram-positive and gram-negative bacteria. *Nanomed Nanotechnol Biol Med* 6:103–109
- Prasher P, Sharma M, Mudila H, Gupta G, Sharma AK, Kumar D, Bakshi HA, Negi P, Kapoor DN, Chellappan DK, Tambuwala MM, Dua K (2020) Emerging trends in clinical implications of

- bio-conjugated silver nanoparticles in drug delivery. *Coll Interface Sci Commun* 35:100244
7. Kim E-S, Hwang G, El-Din MG, Liu Y (2012) Development of nanosilver and multi-walled carbon nanotubes thin-film nanocomposite membrane for enhanced water treatment. *J Membr Sci* 394–395:37–48
 8. Wang X, Mei Y, Li X, Wang M, Cui Z, Lu G-Q (2019) Pressureless sintering of nanosilver paste as die attachment on substrates with ENIG finish for semiconductor applications. *J Alloys Compd* 777:578–585
 9. Loiseau A, Asila V, Boitel-Aullen G, Lam M, Salmain M, Boujday S (2019) Silver-based plasmonic nanoparticles for and their use in biosensing. *Biosensors* 9(2):78
 10. Ahmed HB, Emam HE (2016) Layer by layer assembly of nanosilver for high performance cotton fabrics. *Fibers Polym* 17(3):418–426
 11. Khan A, Khan AAP, Asiri AM, Abu-Zied BM (2016) Green synthesis of thermally stable Ag-rGO-CNT nano composite with high sensing activity. *Compos Part B-Eng* 86:27–35
 12. Rajput K, Raghuvanshi S, Bhatt A, Rai SK, Agrawal PK (2017) A review on synthesis silver nano-particles. *Int J Curr Microbiol Appl Sci* 6(7):1513–1528
 13. Abul Barkat Md, Harshita BS, Naim MJ, Pottoo FH, Singh SP, Ahmad FJ (2018) Current progress in synthesis, characterization and applications of silver nanoparticles: precepts and prospects. *Recent Pat Anti-Infect Drug Discov* 13:53–69
 14. Abu-Zied BM, Asiri AM (2014) An investigation of the thermal decomposition of silver acetate as a precursor for nano-sized Ag-catalyst. *Thermochim Acta* 581:110–117
 15. Jha M, Shimpi NG (2018) Spherical nanosilver: Bio-inspired green synthesis, characterizations, and catalytic applications. *Nano-Struct Nano-Objects* 16:234–249
 16. Dasaradhadu Y, Srinivasan MA (2020) Synthesis and characterization of silver nano particles using co-precipitation method. *Mater Today Proc* 33(1):720–723
 17. Tseng KH, Kao Y-S, Chang C-Y (2016) Development and implementation of a micro-electric discharge machine: real-time monitoring system of fabrication of nanosilver. *Coll J Clust Sci* 27:763–773
 18. Bera P, Patil KC, Hegde MS (2000) NO reduction, CO and hydrocarbon oxidation over combustion synthesized Ag/CeO₂ catalyst. *Phys Chem Chem Phys* 2:3715–3719
 19. Shobha N, Nanda N, Giresha AS, Dharmappa KK, Nagabhushana BM, Mylarappa M (2018) Synthesis and characterization of Ag nano particle by solution combustion method and their biological studies. *Mater Today Proc* 5(10):22614–22620
 20. Zhang D, Pu X, Li H, Yu YM, Shim JJ, Cai P, Sil K, Seo HJ (2015) Microwave-assisted combustion synthesis of Ag/ZnO nanocomposites and their photocatalytic activities under ultraviolet and visible-light irradiation. *Mater Res Bull* 61:321–325
 21. Sharma P, Lotey GS, Singh S, Verma NK (2011) Solution-combustion: the versatile route to synthesize silver nanoparticles. *J Nanopart Res* 13:2553–2561
 22. Shang Z, Yang Z, Xiao Y, Wang X (2020) Ordered mesoporous Ag/CeO₂ nanocrystalline via silica-templated solution combustion for enhanced photocatalytic performance. *Coll Surf A* 604:125301
 23. Abu-Zied BM (2002) Preparation of cadmium chromite spinel: a combustion approach. *Coll Surf A* 211:27–42
 24. Abu-Zied BM (2008) Oxygen evolution over Ag/Fe_xAl_{2-x}O₃ (0.0 ≤ x ≤ 2.0) catalysts via N₂O and H₂O₂ decomposition. *Appl Catal A Gen* 334:234–242
 25. Abu-Zied BM, Asiri AM (2012) Urea based combustion process for the synthesis of nanocrystalline Ni-La-Fe-O catalysts. *J Nanomater* 1:7
 26. Makhoulf MTh, Abu-Zied BM, Mansoure TH (2013) Direct fabrication of cobalt oxide nanoparticles employing sucrose as a combustion fuel. *J Nanopart*. <https://doi.org/10.1155/2013/384350>
 27. Makhoulf MTh, Abu-Zied BM, Mansoure TH (2013) Nanocrystalline Co₃O₄ fabricated via the combustion method. *Metals Mater Int* 19:489–495
 28. Makhoulf MTh, Abu-Zied BM, Mansoure TH (2013) Effect of calcination temperature on the H₂O₂ decomposition activity of nano-crystalline Co₃O₄ prepared by combustion method. *Appl Surf Sci* 274:45–52
 29. Makhoulf MTh, Abu-Zied BM, Mansoure TH (2014) Effect of fuel/oxidizer ratio and the calcination temperature on the preparation of microporous-nanostructured tricobalt tetraoxide. *Adv Powder Technol* 25:560–566
 30. Abu-Zied BM (2019) A novel foam combustion approach for the synthesis of nano-crystalline cobalt oxide powder. *Ceram Int* 45:4540–4548
 31. Amjad U, Sherin L, Zafar MF, Mustafa M (2019) Comparative study on the catalytic degradation of methyl orange by silver nanoparticles synthesized by solution combustion and green synthesis method. *Arab J Sci Eng* 44:9851–9857
 32. Aziz A, Khalid M, Akhtar MS, Nadeem M, Gilani ZA, Ul Huda Khan Asghar HMN, Rehman J, Ullah Z, Saleem M (2018) Structural, morphological and optical investigations of silver nanoparticles synthesized by sol-gel autocombustion method. *Dig J Nanomater Bios* 13(3):679–683
 33. Mikhailov YM, Aleshin VV, Kolesnikova AM, Kovalev DYu, Ponomarev VI (2015) Flameless combustion synthesis of Ni and Ag nanoparticles in ballasted systems: a time-resolved X-ray diffraction study. *Propellants Explos Pyrotech* 40:88–94
 34. Abu-Zied BM, Alamry KA (2019) Green synthesis of 3D hierarchical nanostructured Co₃O₄/carbon catalysts for the application in sodium borohydride hydrolysis. *J Alloys Compd* 798:820–831
 35. Janković B, Stopić S, Bogović J, Friedrich B (2014) Kinetic and thermodynamic investigations of non-isothermal decomposition process of a commercial silver nitrate in an argon atmosphere used as the precursors for ultrasonic spray pyrolysis (USP). The mechanistic approach. *Chem Eng Process* 82:71–87
 36. Wu W, Wu M, Sun Z, Li G, Ma Y, Liu X, Wang X, Chen X (2013) Morphology controllable synthesis of silver nanoparticles: Optical properties study and SERS application. *J Alloys Compd* 579:117–123
 37. Singh N, Khanna PK (2007) *In situ* synthesis of silver nano-particles in polymethylmethacrylate. *Mater Chem Phys* 104:367–372
 38. Stradella L, Argentero M (1993) A study of the thermal decomposition of urea, of related compounds and thiourea using DSC and TG-EGA. *Thermochim Acta* 219:315–323
 39. Schaber PM, Colson J, Higgins S, Thielen D, Anspach B, Brauer J (2004) Thermal decomposition (pyrolysis) of urea in an open reaction vessel. *Thermochim Acta* 424:131–142
 40. Krum K, Patil R, Christensen H, Hashemi H, Wang Z, Li S, Glarborg P, Wu H (2021) Kinetic modeling of urea decomposition and byproduct formation. *Chem Eng Sci* 230:116138
 41. Abu-Zied BM (2019) Controlled synthesis of praseodymium oxide nanoparticles obtained by combustion route: effect of calcination temperature and fuel to oxidizer ratio. *Appl Surf Sci* 471:246–255
 42. Yanase A, Komiyama H, Tanaka K (1990) Adsorbate-induced lattice relaxation of small supported silver particles observed by an in situ X-ray diffraction technique. *Surf Sci Lett* 226:L65–L69
 43. Nagy A, Mestl G (1999) High temperature partial oxidation reactions over silver catalysts. *Appl Catal A Gen* 188(1–2):337–353
 44. Abu-Zied BM (2000) Structural and catalytic activity studies of silver/chromia catalysts. *Appl Catal A Gen* 198:139–153
 45. Lavrenko VA, Malyshevskaya AI, Kuznetsova LI, Litvinenko VF, Pavlikov VN (2006) Features of high-temperature oxidation in air of

- silver and alloy Ag–Cu, and adsorption of oxygen on silver. *Powder Metall Met Ceram* 45(9–10):476–480
46. Hong C, Huan Y, Zhang P, Zhang K, Dai P (2021) Effect of silver content on the microstructure, thermal stability and mechanical properties of CrN_x/Ag nanocomposite films. *Ceram Int* 47(18):25324–25336
 47. Jelić D, Penavin-Škundrić J, Majstorović D, Mentus S (2011) The thermogravimetric study of silver(I) oxide reduction by hydrogen. *Thermochim Acta* 526:252–256
 48. Yi Z, Xu X, Zhang K, Tan X, Li X, Luo J, Ye X, Wu W, Wu J, Yi Y, Tang Y (2013) Green, one-step and template-free synthesis of silver spongelike networks via a solvothermal method. *Mater Chem Phys* 139:794–801
 49. Uemiyama S, Matsuda T, Kikuchi E (1991) Hydrogen permeable palladium-silver alloy membrane supported on porous ceramics. *J Membr Sci* 56:315–325
 50. Bidault F, Kucernak A (2011) Cathode development for alkaline fuel cells based on a porous silver membrane. *J Power Sour* 196:4950–4956
 51. Kawahara K, Tanford C (1966) Viscosity and density of aqueous solutions of urea and guanidine hydrochloride. *J Bio Chem* 241:3228–3232
 52. Du J, Han B, Liu Z, Liu Y (2007) Control synthesis of silver nanosheets, chainlike sheets, and microwires via a simple solvent-thermal method. *Cryst Growth Des* 7(5):900–904
 53. Du FT, Yu PF, Cui B, Cheng HO, Chang ZG (2009) Preparation and characterization of monodisperse Ag nanoparticles doped barium titanate ceramics. *J Alloys Compd* 478:620–623
 54. Abu-Zied BM, Ali TT (2018) Fabrication, characterization and catalytic activity measurements of nanocrystalline Ag–Cr–O catalysts. *Appl Surf Sci* 457:1126–1135
 55. Sun Z, Dong N, Wang K, König D, Nagaiah TC, Sanchez MD, Ludwig A, Cheng X, Schuhmann W, Wang J, Muhler M (2013) Ag-stabilized few-layer graphene dispersions in low boiling point solvents for versatile nonlinear optical applications. *Carbon* 62:182–192
 56. Albitar E, Valenzuela MA, Alfaro S, Valverde-Aguilar G, Martínez-Pallares FM (2015) Photocatalytic deposition of Ag nanoparticles on TiO₂: metal precursor effect on the structural and photoactivity properties. *J Saudi Chem Soc* 19(5):563–573
 57. Narasimharao K, Abu-Zied BM, Alfaifi SY (2021) Cobalt oxide supported multi wall carbon nanotube catalysts for hydrogen production via sodium borohydride hydrolysis. *Int J Hydrogen Energy* 46:6404–6418
 58. Shen X, Wang Q, Wu Q, Guo S, Zhang Z, Sun Z, Liu B, Wang Z, Zhao B, Ding W (2015) CoB supported on Ag-activated TiO₂ as a highly active catalyst for hydrolysis of alkaline NaBH₄ solution. *Energy* 90:464–474
 59. Paladini M, Arzac GM, Godinho V, Hufschmidt D, Jiménezde Haro MC, Beltrán AM, Fernández A (2017) The role of cobalt hydroxide in deactivation of thin film Co-based catalysts for sodium borohydride hydrolysis. *Appl Catal B-Environ* 210:342–351
 60. Durano MM, Tamboli AH, Kim H (2017) Cobalt oxide synthesized using urea precipitation method as catalyst for the hydrolysis of sodium borohydride. *Coll Surf A* 520:355–360
 61. Huff C, Long JM, Heyman A, Abdel-Fattah TM (2018) Palladium nanoparticle multi-walled carbon nanotube composite as catalyst for hydrogen production by the hydrolysis of sodium borohydride. *ACS Appl Energy Mater* 1(9):4635–4640
 62. Huff C, Long JM, Aboulatta A, Heyman A, Abdel-Fattah TM (2017) Silver nanoparticle/multi-walled carbon nanotube composite as catalyst for hydrogen production. *ECS J Solid State Sci Technol* 6(10):M115–M118
 63. Su C-C, Lu M-C, Wang S-L, Huang Y-H (2012) Ruthenium immobilized on Al₂O₃ pellets as a catalyst for hydrogen generation from hydrolysis and methanolysis of sodium borohydride. *RSC Adv* 2:2073–2079
 64. Liao J, Huang H (2020) Magnetic sensitive *Hericium erinaceus* residue chitin/Cu hydrogel nanocomposites for H₂ generation by catalysing NaBH₄ hydrolysis. *Carbohydr Polym* 229:115426
 65. Bond GC, Keane MA, Kral H, Lercher JA (2000) Compensation phenomena in heterogeneous catalysis: general principles and a possible explanation. *Cat Rev Sci Eng* 42:323–383
 66. Wang Y, Li T, Bai S, Qi K, Cao Z, Zhang K, Wu S, Wang D (2016) Catalytic hydrolysis of sodium borohydride via nanostructured cobalt-boron catalysts. *Int J Hydrogen Energy* 41:276–284
 67. Andrieux J, Demirci UB, Miele P (2011) Langmuir-Hinshelwood kinetic model to capture the cobalt nanoparticles-catalyzed hydrolysis of sodium borohydride over a wide temperature range. *Catal Today* 170:13–19
 68. Li Y, Zhang Q, Zhang N, Zhu L, Zheng J, Chen BH (2013) RuRuO₂/C as an efficient catalyst for the sodium borohydride hydrolysis to hydrogen. *Int J Hydrogen Energy* 38:13360–13367
 69. Rakap M, Özkar S (2009) Intrazeolite cobalt(0) nanoclusters as low-cost and reusable catalyst for hydrogen generation from the hydrolysis of sodium borohydride. *Appl Catal B Environ* 91:21–29

Publisher's Note Springer Nature remains neutral with regard to jurisdictional claims in published maps and institutional affiliations.

Authors and Affiliations

Bahaa M. Abu-Zied¹  · Tarek T. Ali²  · Lamia Adly¹ 

✉ Bahaa M. Abu-Zied
babuzied@aun.edu.eg; babuzied@yahoo.com

Tarek T. Ali
tarek_ali@science.sohag.edu.eg

Lamia Adly
ody96@yahoo.com

¹ Chemistry Department, Faculty of Science, Assiut University, Assiut 71516, Egypt

² Chemistry Department, Faculty of Science, Sohag University, P.O.Box 82524, Sohag, Egypt